Journal of Nuclear Materials 400 (2010) 37–45

Contents lists available at ScienceDirect

Journal of Nuclear Materials

journal homepage: www.elsevier.com/locate/jnucmat

Nanoscale characterisation of ODS–Eurofer 97 steel: An atom-probe tomography study

Ceri A. Williams *, Emmanuelle A. Marquis, Alfred Cerezo, George D.W. Smith

Department of Materials, Oxford University, OX1 3PH, UK

ARTICLE INFO

Article history:
Received 24 March 2009
Accepted 11 February 2010

ABSTRACT

Laser-pulsed atom-probe tomography has been used to study the nanoscale features present in an ODS–Eurofer 97 alloy. A core/shell structure was found for particles 5–10 nm in diameter. The particle cores were primarily Y and O, enriched with Mn and Si resulting in a metal (Y, Mn and Si) to oxygen ratio of M:O ~2:3. The ~2 nm thick outer-shell region of the particles exhibited partitioning of V, Cr, Ta, C and N together with the core elements in many cases. Detailed compositional measurements have also been made on the smallest of the yttria-based oxide clusters down to 2 nm in diameter. The 2 nm clusters were found to have a non-stoichiometric oxide composition, enriched in oxygen compared to Y_2O_3, and evidence for the existence of a shell around these smaller particles was found.

1. Introduction

Eurofer 97 steel was developed in the EU as a reduced activation alloy suitable for fusion applications, within the long term programme of the European Fusion Development Agreement. Depending on processing conditions and subsequent heat treatments, it exhibits either a ferritic, or ferritic/martensitic microstructure [1]. Similar to all ferritic/martensitic steels, Eurofer 97 has a low volumetric expansion under irradiation compared with austenitic steels [2,3], making this a promising candidate material for structural components of Generation IV fission reactors and future fusion power plant. The stringent requirements for these structural materials are such that radiation doses of up to 200 dpa and high operating temperatures (>600 °C) are necessary to optimise efficiency of the reactor, during the lifetime of a component.

An oxide dispersion strengthened (ODS) variant of the Eurofer 97 was fabricated by mechanical alloying the powdered alloy with 0.3 wt.% Y_2O_3, resulting in maintained strength up to ~700 °C due to a fine grain size and the presence of nanometre scale oxide particles [4,5]. The ODS particles are also likely to trap transmutant He and act as a sink for point defects. Mechanical testing experiments have shown promising resistance to radiation damage [6,7].

Previous research has used transmission electron microscopy (TEM) to characterise the fine-scale structure of ODS–Eurofer 97. The strengthening oxide particles have been reported to be as small as 2 nm in diameter [1]. High-resolution TEM of oxide particles ~10 nm in diameter has shown the crystal structure to be of Y_2O_3 type [8,9]. A V–Cr–O shell structure 0.5–1.5 nm thick around each ODS particle was detected with analytical TEM (EDX and EELS) using a 1 nm electron probe [10].

Atom-probe tomography (APT) has been used to characterise ODS particles in other reduced activation ferritic/martensitic (RAFM) steels. One RAFM alloy that has been studied extensively using this method is the ODS 12-YWT alloy (Fe–12Cr–3W–0.4Ti and 0.25 wt.% Y_2O_3), however some ambiguity exists over the compositions of the nanoscale Ti-rich yttria-based oxide particles in this material. Larson et al. [11] reported an Fe concentration of ~78% in the clusters in this 12-YWT, whereas Miller et al. subsequently reported levels of ~40% [12], and only 4–8% [13,14]. It is unclear whether the cause of these variations are from materials processing, alloy compositions, inherent material inhomogeneity, or related to the APT technique and the methods by which clusters are defined and local concentrations measured.

Given the important role played by the oxide particles in strengthening ODS–Eurofer 97 and improving resistance to He embrittlement, it is vital that the nature of these particles be fully understood. Only then can any changes that occur as a result of radiation damage be quantified. Determining the composition and structure of the particles will provide insight into possible mechanisms of formation and help develop methods to further optimise processing of desired alloy structures. This work presents some initial results of an APT study of an ODS–Eurofer 97 alloy, with particular focus on the composition of the finest oxygen-rich features. In order to avoid previous uncertainties in how these compositions are determined, we introduce a systematic approach to cluster selection and composition measurements, with the use of simple corrections to existing data analysis techniques.

* Corresponding author. Address: Department of Materials, University of Oxford, Parks Road, Oxford OX1 3PH, UK. Tel.: +44 1865 273634; fax: +44 1865 273789.
E-mail address: ceri.williams@materials.ox.ac.uk (C.A. Williams).

0022-3115/$ - see front matter © 2010 Elsevier B.V. All rights reserved.
doi:10.1016/j.jnucmat.2010.02.007

2. Materials and methods

The nominal alloy composition is quoted in at.% in Table 1 [9]. The material was sourced from Lindau et al. at Forschungszentrum Karlsruhe, Germany. Powder was obtained by gas-atomisation of the alloy (H.C. Starck) and subsequently mechanically alloyed at Plansee with 0.3 wt.% Y_2O_3 powder in an attritor mill. The powder was then canned, degassed and subjected to Hot Isostatic Pressing (HIP) [1]. After HIP, the material was hot-rolled in a series of deformation steps with intermediate annealing to produce a final plate of 6 mm thickness.

TEM samples were obtained from 3 mm disks that were mechanically polished to 0.3 mm thickness, then electropolished using a solution of 2% perchloric acid in methanol at −30 °C. Images were obtained using either a JEOL 3000 microscope operated at 300 kV or an FEI CM20 microscope operated at 200 kV.

$0.5 \times 0.5 \times 20$ mm rods were cut and electropolished into a sharply-pointed needles with an end radius of ~50 nm, as required for APT, using a solution of 2% perchloric acid in 2-butoxyethanol. These specimens were then analysed in an Imago LEAP™ 3000HR under laser pulsing mode (0.3–0.5 nJ energy, <10 μm spot size, 200 kHz repetition rate) at a specimen temperature of 30–50 K. Additional data was obtained using an Oxford Nanoscience 3-D atom probe using voltage pulsing (20% pulse fraction, 20 kHz repetition rate) and a specimen temperature of 60 K. No significant change in composition was noted when changing from laser pulsing mode to voltage pulsing.

Cluster compositions were calculated from atoms selected using a method based on the maximum separation method [15,16]. Core atoms of Y and O are selected using a maximum separation distance (d_{max}) of 0.6–0.85 nm. Clusters are defined as a group of at least N_{min} ($N_{min} = 10$) core atoms within d_{max}. The remaining atoms are included in a cluster if they are positioned within a surround distance $L = 0.5$–0.7 nm of a core atom defining the cluster. The atoms at the interface are then eroded if they are within 0.2–0.4 nm from a matrix atom. The erosion step prevents including a shell of matrix around the cluster. The N_{min}, d_{max} and erosion values are selected using the method outlined in [15]. The surround distance (L) is chosen by examining its effect on the number of core atoms, whilst maintaining $L > 1/\sqrt{2}\, d_{max}$. L corresponds to a distance beyond which the number of core atoms increases linearly (indicating that any further increase will only include excess matrix atoms).

An estimation of feature size is made from the radius of gyration (R_g), that is the average distance between each cluster atom and the centre of mass of the cluster [17]. Note that while this is one of the best ways of comparing dimensions within atom-probe data, it is not representative of the physical size of the particle. Where comparisons between analysis techniques have been made, dimensions have first been converted to the Guinier radius which has been shown to represent precipitate size more accurately [17]. The Guinier radius is related to the radius of gyration by:

$$R_G = \sqrt{\frac{5}{3}} R_g$$

Table 1
Compositional measurements for bulk material (in at.%).

Element	Nominal	Bulk	Matrix
C	0.46	0.22 ± 0.24	0.08 ± 0.002
P	–	0.02 ± 0.01	0.00 ± 0.000
Si	0.11	0.66 ± 0.10	0.16 ± 0.002
O	–	0.34 ± 0.26	0.01 ± 0.000
Mn	0.38	0.35 ± 0.12	0.32 ± 0.003
Fe	Bal	88.76 ± 0.54	90.10 ± 0.016
Cr	8.6	8.86 ± 0.48	8.90 ± 0.016
Co	–	0.02 ± 0.01	0.02 ± 0.001
Y	–	0.12 ± 0.09	0.01 ± 0.001
Ta	0.04	Trace	Trace
V	0.21	0.26 ± 0.06	0.15 ± 0.002
N	–	0.08 ± 0.05	0.02 ± 0.001
W	0.3	0.27 ± 0.09	0.22 ± 0.003

3. Results

3.1. Microstructural observations

Fig. 1 shows the complex grain structure exhibited by this material resulting from the mechanical alloying process. It can be seen that the grain size distribution is wide with typical sizes between 0 and 5 μm, and the large proportion of sub-micron grains allowed many grain boundaries to be analysed within the atom probe sampling volume. Large spherical oxide particles up to 50 nm in diameter were observed as shown in Fig. 2, along with

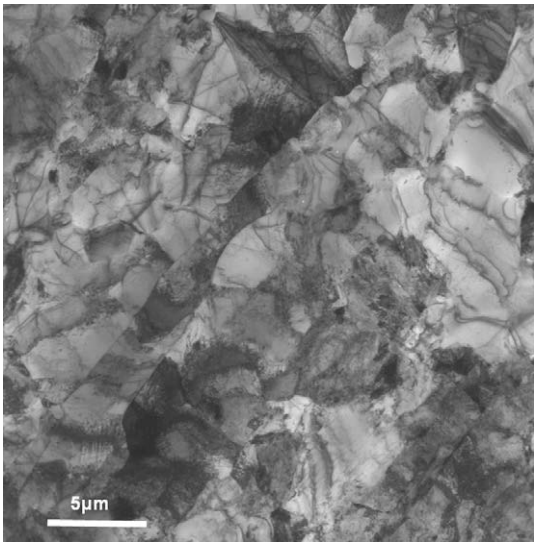

Fig. 1. Bright field TEM image showing complex grain structure.

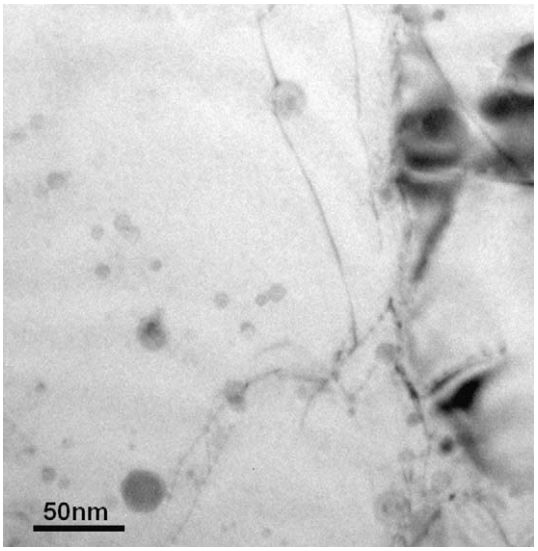

Fig. 2. Bright field TEM image showing oxide particles of varying sizes.

the finer particles seen within grains. The particle distribution is found to be very inhomogeneous, and in ~10% of atom probe specimens, no oxide particles were observed in the regions examined.

Figs. 3 and 4 show alignment of 5–10 nm particles along certain directions. In Fig. 3b, particles are aligned along planar features that could be lath or twin boundaries similar to those shown in the TEM image in Fig. 3a. In Fig. 4, the location of the 5–10 nm oxide particles seen in the APT reconstruction corresponds to the position of the grain boundary seen in the TEM image of the specimen prior to APT analysis. These images also show a uniform distribution of even smaller particles, ~2 nm in diameter within some grains and a particle density of $3.9 \pm 0.15 \times 10^{23}$ m^{-3}. However due

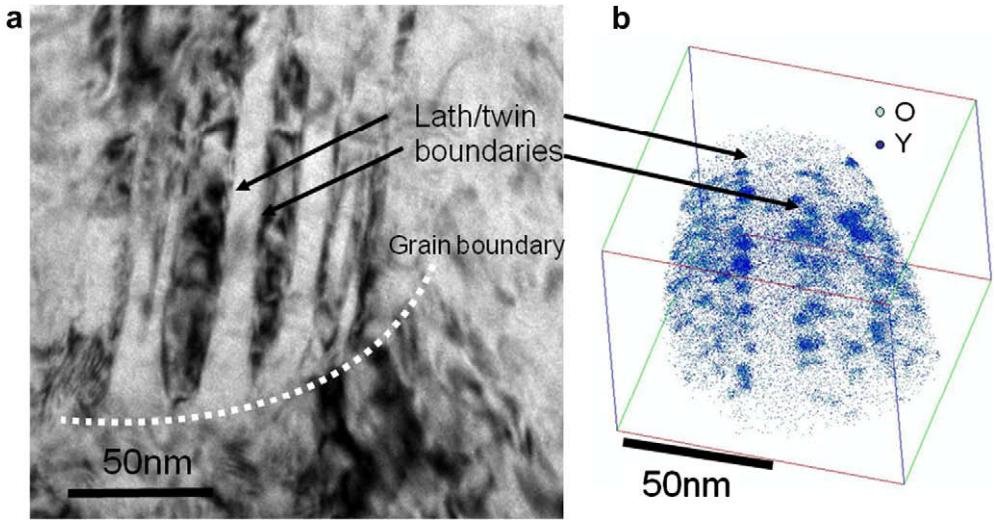

Fig. 3. (a) Bright field TEM image showing possible lath boundaries. (b) APT data showing alignment of yttria-based oxide particles along possible boundaries.

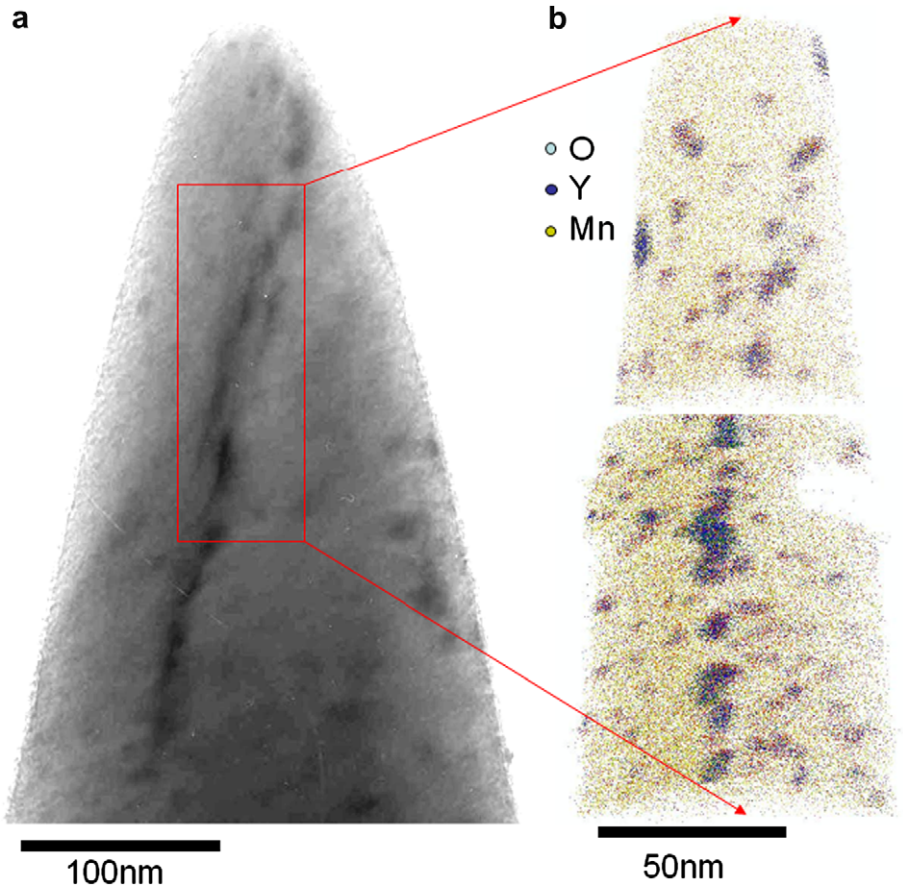

Fig. 4. (a) Bright field TEM image of an APT specimen prior to analysis, showing a grain boundary within the analysis volume. (b) 3-D reconstruction of the APT data obtained from the same tip, with oxide particles present both along the grain boundary and in the bulk material.

to particle-free regions, and regions sparsely populated with larger particles, the overall particle density for the material is less than this value.

3.2. Compositional measurements

Table 1 summarises overall compositional measurements averaged over a number of analysed volumes to account for inherent variations in microstructure from one analysis volume to another. The matrix composition has been estimated from data that showed no particles present in the analysis volume. Although there is good correlation between the nominal composition and the experimental results, several differences are noted. Levels of Ta and C are lower than expected from [18], and traces of P, N, Co and Al were also found. The errors quoted in Table 1 correspond to the standard error of the average composition taken from a large number of separate analyses. This is seen to be greater than the counting statistical error due to the limited volume of analysis and inherent variability within the microstructure.

Table 2
Compositional measurements for 5–10 nm particles (in at.%).

Element	Raw concentration	Matrix-corrected	Oxygen corrected	Range[a]
C	0.50 ± 0.06	1.56 ± 0.19	1.51 ± 0.18	1.01–3.18
P	0.02 ± 0.00	0.06 ± 0.01	0.06 ± 0.01	0.00–0.11
Si	0.92 ± 0.08	2.95 ± 0.27	2.86 ± 0.25	1.55–4.18
O	10.98 ± 0.55	39.74 ± 0.66	41.56 ± 0.58	38.61–45.14
Mn	0.96 ± 0.13	2.52 ± 0.41	2.47 ± 0.42	0.44–5.12
Fe	65.38 ± 0.97	0.00 ± 0.00	0.00 ± 0.00	0.00–0.00
Cr	11.77 ± 0.12	19.70 ± 0.67	19.05 ± 0.53	15.98–21.10
Co	0.03 ± 0.00	0.05 ± 0.01	0.05 ± 0.01	0.03–0.12
Y	4.63 ± 0.27	16.64 ± 0.42	16.19 ± 0.52	15.29–19.35
Ta	0.71 ± 0.13	2.57 ± 0.43	2.50 ± 0.42	0.77–4.93
V	2.91 ± 0.09	10.48 ± 0.52	10.11 ± 0.43	7.66–12.42
N	0.68 ± 0.04	2.43 ± 0.14	2.36 ± 0.14	1.75–3.25
W	0.50 ± 0.03	1.24 ± 0.12	1.20 ± 0.11	0.61–1.54
M:O	8.34 ± 0.54	1.35 ± 0.04	1.19 ± 0.02	1.08–1.37

[a] Corrected compositions.

It has previously been reported that the level of carbon in the alloy is reduced during gas-atomisation of the powder during processing [1] however the results presented here imply an even lower C content than the powder concentration. Due to the low solubility of C in bcc Fe, it can be assumed that the majority of the C is segregated to grain boundaries or other defects such as carbides, not seen in the analysis volume. Carbides have been reported in some studies of ODS–Eurofer [4,19], but not in others [6]. However they were not regularly seen in TEM analysis during this study.

It is shown in the results presented below that Ta is strongly segregated to the oxide particles. Ta is therefore likely to be concentrated in larger oxide particles shown in Fig. 2, but not seen in the analysis volume.

3.2.1. Large particle analysis (5–10 nm)

A 2-D slice of one of the large particles seen in the APT data in Table 2b is given in Fig. 5. A 1-D concentration profile obtained from a cylinder of 7 nm diameter and intercepting a typical particle is shown in Fig. 6. By examining the cross-section and concentration profile, it appears that the particles have a core/shell type structure and it can be seen that the levels of Cr and V are highest near the particle–matrix interface, whereas Y, O, Mn and Si are more concentrated at the core. A number of steps were undertaken to determine the composition of these particles, and the results are summarised in Table 2.

The level of Fe measured in the particles varies from 60% to 75%, with larger particles containing less Fe. While it is possible that the particles contain some Fe, it is thought this very high level is mainly the result of trajectory aberrations known to occur with this type of particle. The oxide particles have been shown to image darkly during field-ion evaporation [20], and so will have a reduced local magnification compared to the surrounding matrix, leading to trajectory overlaps up to a few nanometres near the particle/matrix interface [21]. The relative amount of Fe decreases with increasing particle size and no Fe is present at the core of the larger particles (Fig. 7), a region not affected by trajectory overlap. In order to compare datasets, the amount of Fe will be artificially set to 0 and the matrix contribution can be corrected by calculating the likely proportion of alloying elements present together with Fe in the matrix, and removing this number of atoms from the raw cluster composition. Matrix-corrected compositional values calculated in this way are given in Table 2.

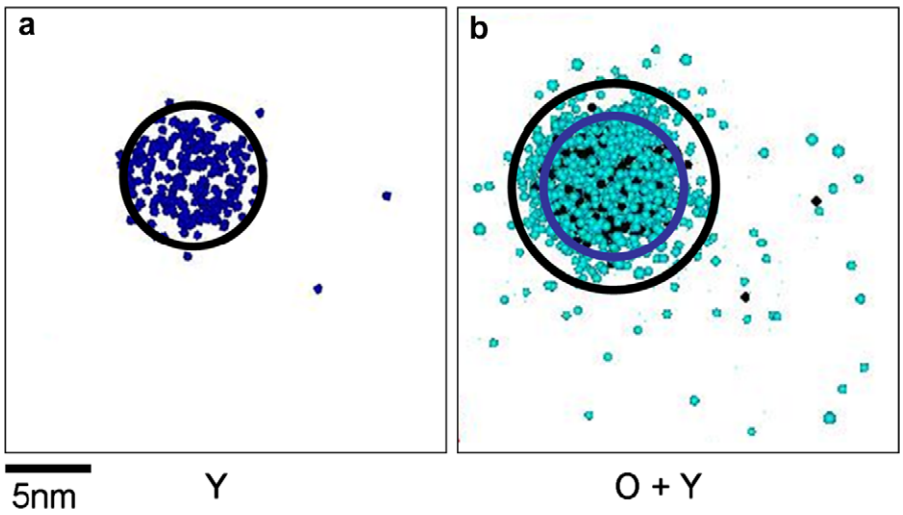

Fig. 5. 2-nm Slice taken from an APT dataset containing a 10 nm particle showing (a) Y atoms (b) O atoms. Schematic rings are drawn in (b) to represent the atoms selected by the cluster selection process (inner ring) and the extra oxygen atoms included by the correction method (outer ring).

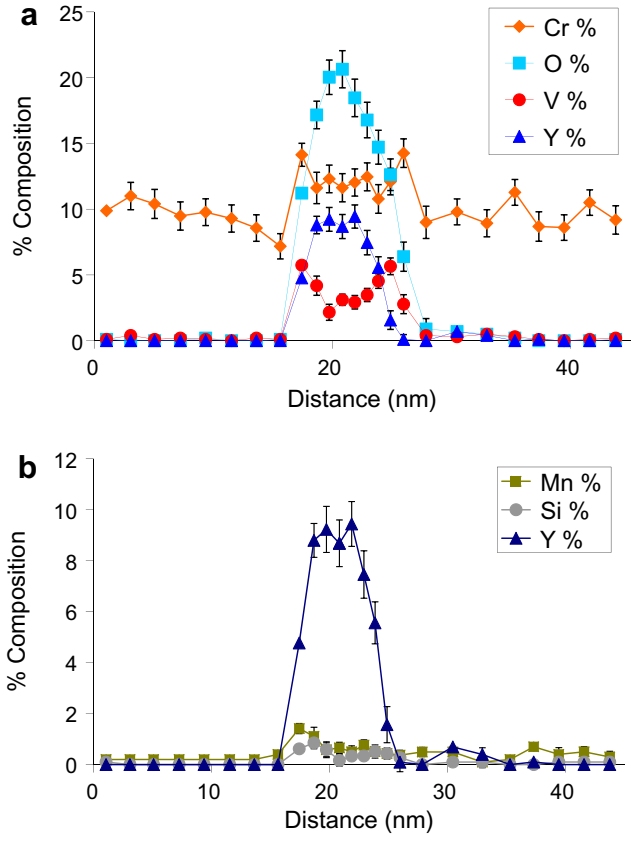

Fig. 6. Composition profile along the direction of analysis, intercepting a representative particle (data obtained from a particle shown in Fig. 3). (a) The Cr and V profiles suggest a shell structure around a Y–O core. (b) Mn and Si are within the particle core.

Miller et al. reported that in the 12-YWT alloy, oxygen atoms in the clusters have a greater R_g than segregated metal atoms. Fig. 5 shows that this is also the case for the larger particles described here, and the distribution of O atoms is much broader than that of the Y atoms. This effect is thought to be due to irregular oxygen evaporation from the tip. Since O atoms are spread more than the maximum separation distance used in the cluster selection, a simple correction was applied to include these atoms. All oxygen atoms found within a sphere of radius equal to the Guinier radius plus 2–2.5 nm (shown schematically in Fig. 5) were included in final corrected composition values in Table 2. Again, the standard error is seen to be significantly larger than the expected statistical error. There is significant variation in composition from one particle to another, and the range of measured composition for each element is indicated. This accounts for the large error in the case of some elements. It is likely that the particle composition varies with diameter, and the presence of grain boundaries near the particles may also affect the composition.

The exact composition of the core and shell could not be determined, as the full width half maximum measurement of the shell thickness for the particle shown in Fig. 7 estimates the layer to be 2 ± 0.5 nm, which is close to the resolution limit of APT for compositional measurements. By increasing the erosion distance to 2–3 nm, the composition of the core of each large particle was estimated, then removed from the total composition of the particle to give an approximate composition for the shell. In many cases, overlap of the core and shell could not be avoided, however the results shown in Table 3 are valuable as it can be seen that over a large number of analysed particles C and N are predominantly found in the shell, as are Cr, V, W and Ta. As it is not possible to correct the oxygen composition without making an assumption on how much oxygen should be included in either the core or shell, oxygen atoms were not included in the results displayed in Table 3.

In one case, a particle 10 nm in diameter was analysed close the surface of a very sharp specimen (end radius ~20 nm). In this instance, the magnification of the particle is greater, and therefore the resolution was improved. A 2-D slice through this particle (2 nm thick) is shown in Fig. 7. For clarity, an iso-concentration surface was created to represent the particle–matrix interface at 25 at.% YO as shown in Fig. 7a. This particular concentration corresponds to the greatest concentration gradient for this interface. In Fig. 7b–d, only atoms inside the iso-concentration surface are shown to represent the particle.

It can be seen that the core of the particle is completely depleted of all elements except Y, O, Mn and Si. The M:O ratio of this particle calculated for a sphere of 2 nm radius at the core is found to be 0.72 ± 0.15, with no oxygen correction applied. This indicates that the particle core is likely to have the reported Y_2O_3 stoichiometry, if it is assumed that some O is lost due to the O spreading problem discussed earlier leading to the M:O ratio appearing slightly above 0.66. It should be noted that the M:O ratio across the core and shell as given in Table 2 as 1.19 ± 0.02, and the possible reasons for this are discussed.

3.2.2. Small cluster analysis

Fig. 8 shows a uniform distribution of small clusters within a grain. As these 2 nm clusters are close to the resolution limit for compositional measurements by atom-probe tomography, careful analysis and interpretation of results is required to understand the effects of technique artefacts on the measured compositions. Cluster composition measurements were carried out using a similar method to that described for the 5–10 nm particles, however to improve counting statistics the total number of atoms for all small clusters in a given analysis volume was used to give the average composition. Raw composition measurements show an apparent level of Fe of 73% in the clusters, which is consistent with the early measurements of 78% Fe in oxide particles within the 12-YWT alloy as published by Larson et al. [11]. As with the 5–10 nm particles, it is assumed that this is the result of trajectory aberrations so the matrix correction is applied using the same method.

The atom maps in Fig. 8 show that the distribution of O atoms is also much broader than that of the Y atoms in the 2 nm particles. Using a maximum separation distance of 1 nm, the R_g for the oxygen atoms in the clusters was measured to be 1.3 ± 0.15 nm, compared with 0.63 ± 0.02 nm for Y atoms. As the 2 nm clusters can be very close together, it is sometimes difficult to assign the spread oxygen atoms to an individual particle, therefore and alternative method to that described for the 5–10 nm particles was necessary. A background noise correction is applied to the mass spectrum, and the level of oxygen in the matrix is estimated from an analysis volume containing no particles (shown in Table 1). The total number of oxygen atoms left after the noise and matrix contributions have been removed is the number used in calculating the average composition of all ~2 nm clusters in a given analysis volume. Every effort has been made to ensure that the cluster is accurately defined so that this oxygen correction can be applied with confidence, and reproducible results have been obtained. As shown in Table 4., the final metal to oxygen ratio in the particles is 0.54 ± 0.04 once all these corrections are applied. A non-stoichiometric oxide composition is therefore implied from these results, with an excess of oxygen when compared with Y_2O_3.

Comparing compositions given in Table 4, it can be seen that the clusters show similar segregation to the 5–10 nm particles, and are particularly enriched in Y, Cr, V, Si and Ta. Notably, no significant enrichment of Mn was detected in the 2 nm clusters. The

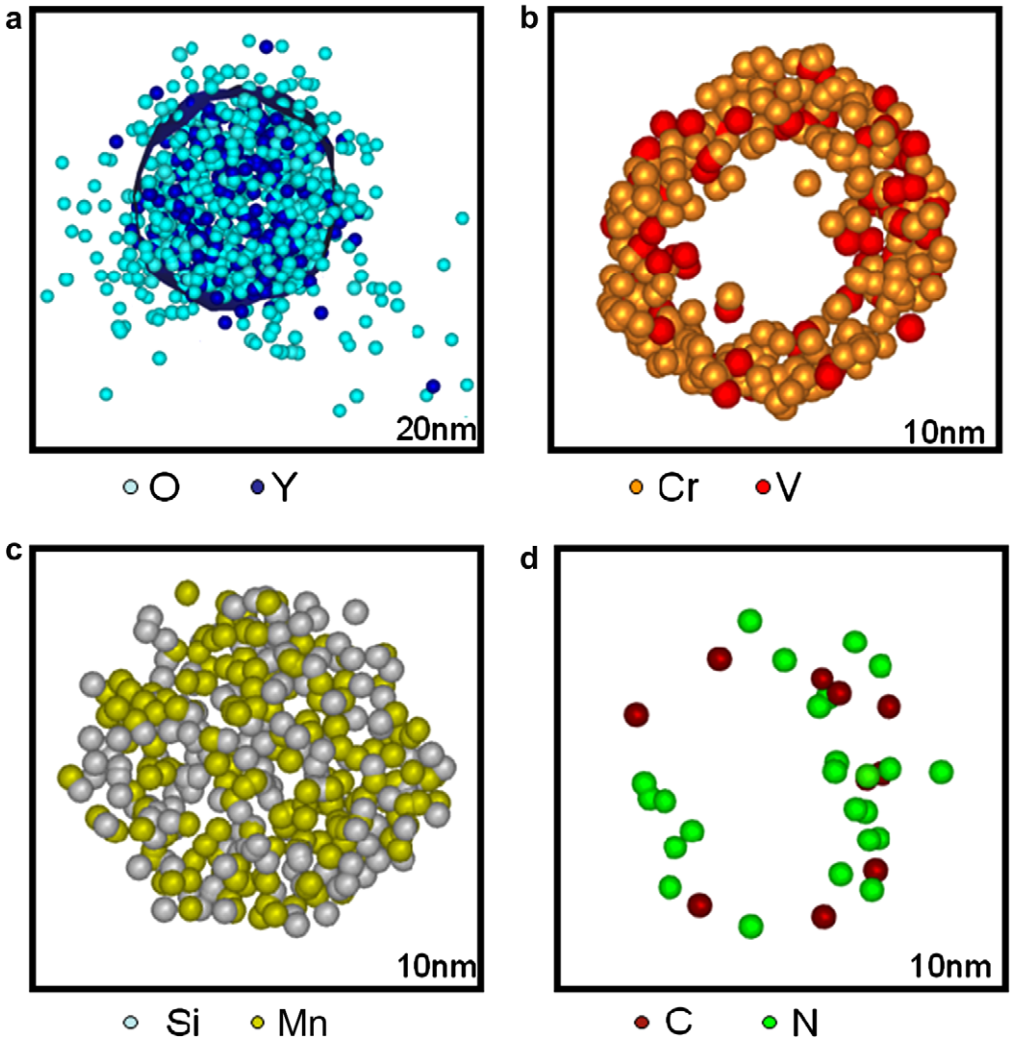

Fig. 7. (a) The 25% concentration Y–O isosurface is drawn on a 2 nm slice through the 10 nm particle shown. (b) The V and Cr atoms inside the iso-concentration surface are present only near the particle–matrix interface. (c) All Mn and Si atoms inside the isosurface are shown (taken from the same section of the particle). Their presence at the core of the particle is clearly visible. (d) C and N are also only present in the particle shell (in this case a 5 nm slice was used to include more atoms).

Table 3
Compositional measurements for the core and shell of 5–10 nm particles (in at.%).

Element	Core composition (%)	Shell composition (%)
C	2.24 ± 0.34	2.71 ± 0.28
P	0.08 ± 0.03	0.11 ± 0.02
Si	4.06 ± 0.53	5.18 ± 0.42
O	0.00 ± 0.00	0.00 ± 0.00
Mn	4.78 ± 0.84	3.92 ± 0.60
Fe	0.00 ± 0.00	0.00 ± 0.00
Cr	30.36 ± 1.26	33.57 ± 0.60
Co	0.02 ± 0.01	0.12 ± 0.02
Y	33.77 ± 0.82	25.43 ± 0.68
Ta	3.89 ± 0.85	4.48 ± 0.74
V	16.27 ± 0.72	17.69 ± 0.73
N	3.92 ± 0.24	4.08 ± 0.24
W	1.57 ± 0.31	2.22 ± 0.20

calculated R_g values for individual elements show differences, as seen in Table 5. This indicates an inhomogeneous distribution of metal atoms within the particle, with V and Cr seen systematically further from the core than the Y atoms. This suggests the 2 nm clusters also consist of a V/Cr shell around a Y rich core – as seen in the 5–10 nm particles.

4. Discussion

The results described above show the detailed composition of the oxide clusters in ODS–Eurofer 97 as measured using APT. A high density of 2 nm oxide particles is observed in the bulk and larger oxide particles (5–10 nm) are seen predominately at grain boundaries. An yttria-rich core, surrounded by a Cr- and V-rich shell was found for all oxide particles. Mechanisms of formation of the clusters, and possible reasons for the existence of the core/shell structure will now be discussed, and compared to what is currently known about oxide clusters in similar ODS alloys.

There are two plausible theories for the existence of the core/shell structure. The first theory is that the shell is a result of segregation to the particle/matrix interface after the particle has formed. The second argument is that the shell could be essential to the formation of the particle, and may act as an interfacial phase, lowering the surface energy of the particle, thus allowing the particle to form.

The results indicate that the larger particles exhibit the most stable oxide composition – Y_2O_3 and APT analysis of a 2 nm sphere at the core of the particle shown in Fig. 7 gives an M:O ratio of 0.72 ± 0.15. Previous TEM observations have also shown the core of these particles to have Y_2O_3 stoichiometry [8]. The combined

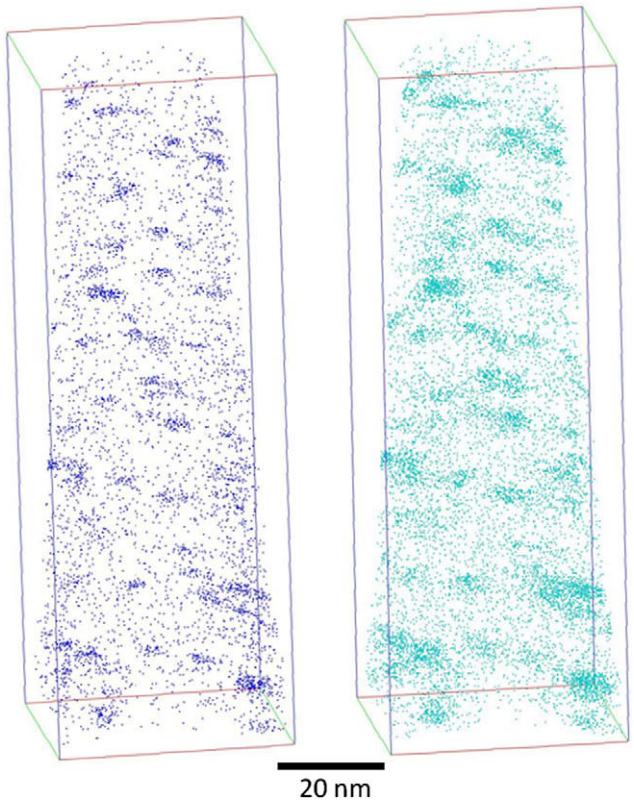

Fig. 8. 3-D reconstruction of APT data showing an even distribution of small ~2 nm particles. Image shows the spread of oxygen atoms (b) compared to yttrium (a) in 3-D reconstruction of atom-probe data.

core and shell compositions shown in Table 2, however, gives a metal to oxide ratio of 1.19:1 for the 5–10 nm particles, which is non-stoichiometric with oxygen deficiency.

The composition profile of a typical particle seen in Fig. 6 shows that the Cr peak from the shell is mainly outside the O profile, suggesting interfacial segregation. It may therefore increase the metal content of the particle (core and shell) to give the ~1:1 M:O ratio. The presence of some oxygen in the shell is also detected in the APT data, however this could be due to the artefacts discussed in Section 3.2.1, and caused by a spread of oxygen from the core. More work is underway to attempt to quantify how much oxygen may be present in the shell, and to establish whether there is any loss of detection efficiency in the clusters due to multiple detector hits (and whether this affects the oxygen concentration particularly).

Table 4
Average cluster compositions for ~2 nm clusters (in at.%).

Element	Overall	Raw concentration	Matrix-corrected	Oxygen corrected
C	0.16 ± 0.15	0.38 ± 0.22	1.38 ± 0.72	0.79 ± 0.47
P	0.02 ± 0.01	0.05 ± 0.00	0.20 ± 0.06	0.11 ± 0.04
Si	0.32 ± 0.01	0.51 ± 0.04	1.36 ± 0.12	0.77 ± 0.06
O	0.23 ± 0.05	6.29 ± 0.51	33.92 ± 2.16	62.68 ± 1.49
Mn	0.30 ± 0.03	0.33 ± 0.04	0.45 ± 0.16	0.26 ± 0.08
Fe	89.01 ± 0.24	72.93 ± 2.21	0.00 ± 0.00	0.00 ± 0.00
Cr	9.04 ± 0.34	11.28 ± 0.29	21.60 ± 1.44	12.25 ± 1.69
Co	0.03 ± 0.00	0.02 ± 0.00	0.00 ± 0.00	0.00 ± 0.00
Y	0.07 ± 0.01	2.53 ± 0.24	13.92 ± 2.85	7.94 ± 2.22
Ta	0.01 ± 0.00	0.35 ± 0.05	1.88 ± 0.13	1.06 ± 0.14
V	0.25 ± 0.02	4.15 ± 1.55	21.38 ± 6.15	11.93 ± 2.76
N	0.12 ± 0.00	0.69 ± 0.23	3.20 ± 0.87	1.79 ± 0.38
W	0.43 ± 0.07	0.48 ± 0.05	0.71 ± 0.10	0.40 ± 0.08
M:O		14.71 ± 1.25	1.77 ± 0.16	0.54 ± 0.04

Table 5
R_g values for 2 nm clusters.

Element	Average, R_g (nm)
All	0.8 ± 0.07
Y	0.56 ± 0.016
V	0.85 ± 0.025

Table 6
Enthalpy of formation of pure binary oxides of selected solute species (at °C) [34].

Element	Oxide composition	ΔHf (kJ/mol (Oxide))	ΔHf (kJ/mol O)
Y	Y_2O_3	1907	636
Cr	Cr_2O_3	1130	377
Si	SiO_2	911	456
V	V_2O_5	1551	310
	VO	432	432
Ta	Ta_2O_5	2047	409
Mn	Mn_3O_4	1388	347
	MnO	385	385
Fe	Fe_3O_4	1118	280
	Fe_2O_3	822	274

All the metallic species seen partitioned to the oxide particles correspond to elements with a high affinity for oxygen. Table 6 shows that for all elements segregated to the clusters/particles, the enthalpy of formation of oxide is lower than that of Fe. It is expected that the oxide particles will mainly be based on Y, due to the larger enthalpy of formation for yttrium-oxide. Cr and V have affinities for O only slightly below that of Y, and it is known that Y_2O_3 and V_2O_3 are isostructural [22], therefore, Cr and V are expected to form part of the oxide. However, these two elements are predominately found at the particle–matrix interface. It is interesting to note that Mn and Si are observed in higher concentrations at the core of the particle, and that the native oxides of both these species are structurally different from Y_2O_3. The oxidation enthalpies of Mn and Si are also lower than Y, Cr and V, which could influence the segregation behaviour.

If the existence of a shell was purely the result of interfacial segregation, it would be expected that as the particles decrease in diameter, the proportion of metal would increase. An important observation reported in the results above is that the smallest oxide clusters are enriched in oxygen compared with those above 5 nm in diameter. The method used to calculate the composition of these clusters is one possible reason that could account for this discrepancy. Indeed, by artificially setting Fe = 0, we may have removed too many metal species forming the small clusters. Alternatively, due to the Gibbs–Thompson effect, the oxygen concentration in the matrix may be increased when small particles are present, and this extra oxygen may have been incorrectly included during the cluster selection process. The M:O ratio is approximately 1:2 in the 2 nm particles, whereas for the 5–10 nm particles it is approximately 1:1 when calculated for the core and shell combined. As this difference is relatively large, it is more likely that there is a difference in stoichiometry between the smallest clusters and those above 5 nm in diameter. A mixed oxide phase in the shell could also explain the size dependency of the M:O ratio.

If the core and shell of the 2 nm clusters are to be thought of as a mixed oxide phase, this structure can be discussed in terms of cluster nucleation. It is however important to remember that dissolution and nucleation mechanisms may vary as function of alloy composition and processing parameters. Lindau et al. have sug-

gested that the particles may be remnant Y_2O_3 powder particles not fully dissolved and made spherical by surface diffusion acting to lower the free energy of the interface [1]. This mechanism would be consistent with the segregation of alloying elements to the cluster interface and contributing to lowering the interface energy.

It is now presumed that yttria is forced into a supersaturated solid solution during milling, then re-form at a later stage [23–25]. X-ray diffraction [24] and small-angled neutron scattering [25] measurements have shown the complete dissolution of the Y_2O_3 powder during milling occurs in similar ODS alloys, and it is assumed that oxide clusters are nucleated during the HIP treatment [25–28]. It is known that O has a very low solubility in Fe [29], therefore the formation of the oxide particles from a supersaturated solid solution created by mechanical alloying is unsurprising. The oxide particles at boundaries are larger than the clusters in the bulk are likely to be the result of fast diffusion along lath/grain boundaries, accelerated during HIP. Given the inhomogeneous nature of the alloy mentioned in Section 3.1, it possible that in localized areas there is limited dissolution. It is unclear from these results as to whether any of the observed particles are the result of remnant powder.

Despite compositional variations, ODS-RAFM alloys all show a dispersion of oxide particles rich in Y and O. In alloys that contain Ti, the particles are also rich in Ti [6,12–14]. A finer dispersion is achieved on the addition of Ti [11] and it has also been shown that elements such as Hf and Zr act in a similar manner [27,30]. It is proposed by Ratti et al. that the primary function of Ti is to enhance the coarsening resistance of the clusters [31]. However, another study carried out using APT reports a Ti-rich shell around Y-based oxide particles in another ODS steel, and it was suggested that Ti assists the nucleation of Y_2O_3 [26]. In all cases where Ti is included in the alloy, it is concluded that the Ti is part of the oxide phase. There is however a marked difference in M:O ratio comparing the results in this paper with Ti containing alloys analysed using APT [11–14]. The ~2 nm ODS clusters in Eurofer give a ~1:2 ratio compared to ~1:1 in the Ti-rich clusters [13,14]. Given that there are multiple known stable phases in the Ti–O system [32], it is very likely that the presence of Ti in these alloys yields a different oxide composition. However due to the differences in cluster composition calculations, and possible differences in the evaporation sequences of the complex ions containing Ti/O it is possible that these effects may account for part of the discrepancy.

Having studied the conclusions of others investigating similar ODS alloys, it appears that the theories proposed for the formation of oxide clusters containing Ti can be applied to the ODS–Eurofer alloy system. For example, where the Ti containing oxide shell is thought to assist in the formation of oxide clusters, a similar effect may occur in the ODS–Eurofer, but with a Cr/V oxide. One reason for this could be that the Cr/V oxide acts as an interfacial phase lowering the interfacial energy, so as to allow the yttria-based phase to form. Similar effects of wetting have been observed in other alloy systems [33].

5. Conclusions

APT and electron microscopy was used to investigate the nanoscale features of the ODS–Eurofer 97 alloy. Correction methods for an existing cluster selection technique were developed and new insights into the nature of the oxide nanoclusters were found. A core/shell structure was shown to be likely in clusters as small as 2 nm in diameter. TEM reports of a V/Cr rich shell were confirmed for particles 5–10 nm in diameter [10], and it was shown that C, N, Ta and W are also predominantly in the shell along with traces of the core elements. The core of the 5–10 nm particles were found to be primarily Y and O with 5–10% Mn and 5–10% Si. The M:O ratio in the particles was seen to increase from ~1:2 to >1:1 as the radius of the particles increased, and this is possibly due to a change in chemical stoichiometry. Further work is currently underway to look at the effect of irradiation on the oxide particles to help determine the suitability of the material for fusion applications.

Acknowledgements

The authors gratefully acknowledge R. Lindau (Forschungszentrum Karlsruhe, Germany) and R. Faulkner (Loughborough University, UK) for supply of the material. This work was partially supported by UK Engineering and Physical Sciences Research Council (EPSRC) under Grant Number EP/077664/1. CAW is funded under the EPSRC DTA program and EAM acknowledges the Royal Society for funding.

References

[1] R. Lindau, A. Moslang, M. Schirra, P. Schlossmacher, M. Klimenkov, Journal of Nuclear Materials 307 (2002) 769–772.
[2] R.L. Klueh, International Materials Reviews 50 (2005) 287–310.
[3] G.R. Odette, Journal of Nuclear Materials 155 (1988) 921–927.
[4] R. Schaeublin, T. Leguey, P. Spatig, N. Baluc, M. Victoria, Journal of Nuclear Materials 307 (2002) 778–782.
[5] N. Baluc, D.S. Gelles, S. Jitsukawa, A. Kimura, R.L. Klueh, G.R. Odette, B. van der Schaaf, J.N. Yu, Journal of Nuclear Materials 367 (2007) 3–41.
[6] R. Schaublin, A. Ramar, N. Baluc, V. de Castro, M.A. Monge, T. Leguey, N. Schmid, C. Bonjour, Journal of Nuclear Materials 351 (2006) 247–260.
[7] A. Alamo, J.L. Bertin, V.K. Shamardin, P. Wident, Journal of Nuclear Materials 367 (2007) 54–59.
[8] M. Klimiankou, R. Lindau, A. Moslang, Journal of Crystal Growth 249 (2003) 381–387.
[9] M. Klimiankou, R. Lindau, A. Moslang, Journal of Nuclear Materials 329–333 (2004) 347–351.
[10] M. Klimenkov, R. Lindau, A. Moslang, Journal of Nuclear Materials 386 (2009) 553–556.
[11] D.J. Larson, P.J. Maziasz, I.S. Kim, K. Miyahara, Scripta Materialia 44 (2001) 359–364.
[12] M.K. Miller, E.A. Kenik, K.F. Russell, L. Heatherly, D.T. Hoelzer, P.J. Maziasz, Materials Science and Engineering A – Structural Materials Properties Microstructure and Processing 353 (2003) 140–145.
[13] M.K. Miller, D.T. Hoelzer, E.A. Kenik, K.F. Russell, Intermetallics 13 (2005) 387–392.
[14] M.K. Miller, K.F. Russell, D.T. Hoelzer, Journal of Nuclear Materials 351 (2006) 261–268.
[15] D. Vaumousse, A. Cerezo, P.J. Warren, Ultramicroscopy 95 (2003) 215–221.
[16] J.M. Hyde, C.A. English, in: G.E. Lucas, M.A. Kirk Jr., R.G. Elliman (Eds.), Proceedings of the MRS 2000 Fall Meeting, Symposium R: Microstructural Processes in Irradiated Materials, vol. 650, Materials Research Society, Boston, MA/Pittsburgh, PA, 2000/2001, p. R6.6.1.
[17] M.K. Miller, Atom Probe Tomography, Kluwer Academic/Plenum, New York, 2000.
[18] R. Lindau, M. Schirra, Fusion Engineering and Design 58–59 (2001) 781–785.
[19] M. Klimiankou, R. Lindau, A. Moslang, Journal of Nuclear Materials 367 (2007) 173–178.
[20] E.A. Marquis, Applied Physics Letters 93 (2008).
[21] M. Miller, A. Cerezo, M. Heatherington, G.D.W. Smith, Atom Probe Field Ion Microscopy, OUP, 1996.
[22] R. Kiessling, N. Lange, Non-metallic Inclusions in Steel, first ed., vol. II, Iron and Steel Institute, London, 1966.
[23] M.J. Alinger et al., Materials Science and Engineering A – Structural Materials Properties Microstructure and Processing 518 (2009) 150–157.
[24] T. Okuda, M. Fujiwara, Journal of Materials Science Letters 14 (1995) 1600–1603.
[25] M.J. Alinger, S.C. Glade, B.D. Wirth, G.R. Odette, T. Toyama, Y. Nagai, M. Hasegawa, Journal of Nuclear Materials 329 (2004) 382–386.
[26] K. Oka, S. Ohnuki, S. Yamashita, N. Akasaka, S. Ohtsuka, H. Tanigawa, Materials Transactions 48 (2007) 2563–2566.
[27] S. Ukai, M. Fujiwara, Journal of Nuclear Materials 307 (2002) 749–757.
[28] M.J. Alinger, G.R. Odette, D.T. Hoelzer, The development and stability of Y–Ti–O nanoclusters in mechanically alloyed Fe–Cr based ferritic alloys, in: 11th International Conference on Fusion Reactor Materials (ICFRM), Kyoto, Japan, 2003, pp. 382–386.
[29] J.T. Swisher, Transactions of the Metallurgical Society AIME 239 (1967) 4.
[30] S.O.Y. Uchida, N. Hashimoto, T. Suda, T. Nagai, T. Shibayama, K. Hamada, N. Akasaka, S. Yamashita, S. Ohstuka, T. Yoshitake, Effect of minor alloying

element on dispersing nano-particles in ODS steels, in: Proceedings of the 2006 MRS Fall Meeting, International Microscopy Congress, Sapporo.
[31] M. Ratti, D. Leuvrey, M.H. Mathon, Y. de Carlan, Journal of Nuclear Materials 386 (2009) 540–543.
[32] T.B. Massalski (Ed.), Binary Alloy Phase Diagrams, second ed., ASM International, 1990.
[33] A. Cerezo, S. Hirosawa, I. Rozdilsky, G.D.W. Smith, Philosophical Transactions of the Royal Society of London Series A – Mathematical Physical and Engineering Sciences 361 (2003) 463–476.
[34] W. Gale, T. Totemeier, Smithells Metals Reference Book, eighth ed., Elsevier, 2004.